Original Research Article

Computational Fluid Dynamics Analysis of Traditional and Laminar Flow Airfoils

Qasim Khan

Repton School Dubai, Nad Al Sheba 3, P.O. Box 300331, Dubai, United Arab Emirates

ABSTRACT

In this study, a comparative Computational Fluid Dynamics (CFD) analysis is presented with the aim of elucidating performance trade-offs between traditional airfoils and laminar flow airfoil designs. Two conventional sections (NACA 2412 and NACA 0012) and two laminar flow designs (NACA 64A010 and NACA 747A315) were analyzed using steady-state Reynolds-Averaged Navier–Stokes (RANS) simulations in ANSYS Fluent employing the SST turbulence model. A mesh refinement study confirmed grid convergence and established mesh independence, with the near-wall resolution maintained at $y^+ \leq 1$. Furthermore, results obtained from the simulations were validated against experimental data and demonstrated strong agreement. Across all Reynolds numbers under investigation (5×10^4, 5×10^5, 2×10^6, and 9×10^6), traditional airfoils achieved superior aerodynamic efficiency, with the NACA 2412 exhibiting the highest lift-to-drag ratios ($C_L/C_D \approx 90$ at $Re = 9 \times 10^6$), while laminar flow profiles demonstrated lower maximum lift. Post-stall behavior revealed slower lift decay for laminar flow sections, indicating improved stall recovery. Overall, the findings suggest that traditional airfoils maintain broader operational efficiency and robustness across varying flow conditions. These conclusions, however, cannot be generalized to all traditional and laminar flow airfoils, as only two airfoils from each category were examined. Additionally, all simulations were performed using a fully turbulent RANS framework without an explicit transition model, which may influence the predicted performance of laminar flow airfoils. The study underscores the significance of airfoil selection for optimizing aircraft performance and highlights the need for future work involving turbulence modeling, three-dimensional effects, and experimental validation to refine our understanding of traditional and laminar flow airfoils.

Keywords: Computational Fluid Dynamics (CFD); Airfoil Aerodynamics; Laminar Flow Airfoils; Traditional Airfoils; Reynolds-Averaged Navier–Stokes (RANS); $k - \omega$ SST Turbulence Model; Aerodynamic Efficiency

INTRODUCTION

One of the most ubiquitous shapes in aviation is the airfoil. Characterized by a distinctive teardrop shape, airfoils are the two-dimensional cross section of a wing, and their geometry is specifically designed to modulate airflow around them to generate lift (1). Governing the aerodynamics of various fields as diverse as unmanned aerial vehicles (UAVs), planes, and supersonic jets, airfoils underpin the design of propellers, wind turbine

Corresponding author: Qasim Khan, E-mail: qasimkhan071007@gmail.com.

Accepted January 9, 2026
https://doi.org/10.70251/HYJR2348.41299309

blades, and motorsport components (1). Hence, airfoils are of particular interest to aerospace engineers, as optimizing these airfoil profiles can significantly enhance their efficiency by reducing drag. In the context of aircraft, this optimization is especially relevant to improve fuel economy and lower travel costs (2). Airfoils are shaped differently to suit differing applications as different shapes have differing aerodynamic characteristics (3). Aerobatic planes and some UAVs may need to execute sharp, steep maneuvers, deliberately operating at high angles of attack (α) to generate sufficient lift (4). Therefore, an airfoil made with the intent to provide a high stall angle would allow aircraft to perform these stunts and fly slower without stalling. The principal objective of most general aviation aircraft, however, is to maintain an optimal cruise efficiency, but there exists a trade-off between conventional airfoils, which have a broad lift range but experience a high drag penalty compared to laminar flow airfoils which have a low drag profile but possess a narrow lift range (5).

According to Abbott and von Doenhoff (3), the earlier, more conventional NACA 4- and 5-series airfoil families are characterized by relatively high drag compared to the laminar flow NACA 6- and 7-series designs, which could maintain a greater extent of laminar flow along their upper surface. Whilst earlier, traditional airfoils featured more reliable lift and stall characteristics, they tend to have higher drag coefficients in contrast to modern laminar flow airfoils, which boast a lower drag coefficient. Despite information being known regarding the differences between traditional and laminar flow airfoils, more comprehensive comparative assessments using one consistent setup that directly provides side-by-side results for conventional and laminar flow airfoils is lacking. Addressing this gap serves to provide insight on how traditional and laminar flow airfoils compare when subjected to the same flight conditions. It is not obvious how a laminar flow airfoil design would perform against a traditional airfoil over the variety of flight conditions being investigated. For example, it is reasonable to suspect that laminar flow airfoils may produce lower drag at standard cruise lift coefficients (3). However, lower drag may not persist at low Reynolds numbers (6). Furthermore, geometries designed to promote laminar flow may experience flow separation and transition to turbulent flow at shallower angles of attack, negating the benefits of any drag reduction (6). The present study hopes to elucidate these performance trade-offs between traditional and laminar flow airfoils. Achieving this would help inform decisions regarding airfoil selection for different flight regimes.

To this end, two traditional airfoils (NACA 2412 and NACA 0012) and two laminar flow airfoils (NACA 64A010 and NACA 747A315) were studied by performing numerical simulations in Ansys Fluent. These airfoil geometries were chosen because they are well-documented in existing literature and thus serve as representative benchmarks for traditional and laminar flow airfoils. Aerodynamically relevant quantities such as the coefficients of lift, drag, and their ratio was used to quantify and assess the performance of the airfoils. While the study is limited to just four airfoils, it provides a useful starting point for drawing comparisons between conventional sections and laminar flow designs. The extent of applicability is therefore constrained to two-dimensional airfoil sections with similar characteristics as the airfoils under investigation at the tested Reynolds numbers. Moreover, although numerical solutions are inherently simplifications of real-world conditions, the use of Computational Fluid Dynamics (CFD) is widely accepted in industry when presented with appropriate validation.

METHODS AND MATERIALS

Computational Fluid Dynamics and Governing Equations

CFD is a method of solving complex physical phenomenon (usually involving a set of partial differential equations) including fluid flow, heat transfer, and chemical reactions by means of computer-based simulation using a numerical algorithm (7). This study used CFD simulations conducted in Ansys Fluent to predict the fluid flow over the relevant airfoils being investigated. The numerical method employed by Fluent is the Finite Volume Method which involves subdividing the fluid flow domain into small, discrete control volumes. The governing equations are integrated over all the cells to ensure important physical quantities are conserved (mass, momentum, energy etc.) in the discrete numerical solution (7).

The equations which govern fluid flow are the incompressible Navier–Stokes equations which is presented as follows,

$$\frac{\partial u_i}{\partial x_i} = 0 \qquad \text{(Eq. 1)}$$

$$\frac{\partial u_i}{\partial t} + u_j \frac{\partial u_i}{\partial x_j} = -\frac{1}{\rho}\frac{\partial p}{\partial x_i} + \nu \frac{\partial^2 u_i}{\partial x_j \partial x_j} \qquad \text{(Eq. 2)}$$

where u_i are the velocity components (m s^{-1}), x_i are the spatial coordinates (m), p is the pressure (Pa), ρ is the fluid density (kg m^{-3}), ν is the kinematic viscosity (m^2 s^{-1}), and the summation convention applies over repeated indices. Eq. 1 represents the continuity equation, enforcing mass conservation while Eq. 2 enforces momentum conservation (7).

While Eq. 1 and Eq. 2 exactly describe the instantaneous flow fields, solving them directly for the turbulent flows is computationally prohibitive due to the extensive spatial and temporal scales involved (8). Consequently, to simplify the problem, Ansys uses the Reynolds-Averaged Navier–Stokes equations (RANS), in which the velocity and pressure flow variables are decomposed into mean time-averaged and fluctuating components as shown in Eq. 3.

$$u_i = \overline{u_i} + u_i', p = \overline{p} + p' \quad \text{(Eq. 3)}$$

Here, u_i' and p_i' denote the fluctuating components of velocity (m s^{-1}) and pressure (Pa), respectively. By substituting these expressions into the Navier–Stokes equations, and taking a time average, the ensemble-averaged momentum equation is derived, which can be represented in Eq. 4 and Eq. 5 in cartesian tensor form. These equations are the governing equations for RANS (9).

$$\frac{\partial \rho}{\partial t} + \frac{\partial}{\partial x_i}(\rho \overline{u_i}) = 0 \quad \text{(Eq. 4)}$$

$$\frac{\partial}{\partial t}(\rho \overline{u_i}) + \frac{\partial}{\partial x_j}\left(\rho \overline{u_i}\,\overline{u_j}\right) = -\frac{\partial \overline{p}}{\partial x_i} + \frac{\partial}{\partial x_j}\left[\mu\left(\frac{\partial \overline{u_i}}{\partial x_j} + \frac{\partial \overline{u_j}}{\partial x_i} - \frac{2}{3}\delta_{ij}\frac{\partial \overline{u_l}}{\partial x_l}\right)\right] + \frac{\partial}{\partial x_j}\left(-\rho \overline{u_i' u_j'}\right) \quad \text{(Eq. 5)}$$

In Eq. 5, μ is the dynamic viscosity (Pa s) and δ_{ij} is the Kronecker delta (dimensionless). The RANS equations introduce the new term $-\rho \overline{u_i' u_j'}$ (τ_{ij}), which is referred to as the Reynolds stress tensor (measured in Pa). This expression contributes turbulent motion to the mean stress tensor. The term presents six unknowns in addition to the mean flow variables, thereby creating a closure problem. Hence, there is a need to find a relation between the Reynolds stress tensor and the mean flow quantities through a turbulence model (10). To achieve closure, most RANS models — including the one used in this study — invoke the Boussinesq hypothesis, which relates the Reynolds stresses to the mean strain rate tensor:

$$\tau_{ij} = 2\mu_t \overline{S}_{ij} - \frac{2}{3}\rho k\, \delta_{ij} \quad \text{(Eq. 6)}$$

Here, μ_t is the effective turbulent viscosity (kg m^{-1} s^{-1}), $\overline{S}_{ij}$ is the mean strain-rate tensor (s^{-1}) and k is the turbulent kinetic energy (m^2 s^{-2}). The computation of μ_t requires additional transport equations for turbulence quantities. This study employs the Shear Stress Transport (SST) $k-\omega$ model, which solves two transport equations: one for turbulent kinetic energy k and one for the specific dissipation rate ω shown in Eq. 7 and Eq. 8, respectively (11); the turbulent kinetic viscosity μ_t can then be calculated from k and ω in Eq. 9 (9).

$$\frac{\partial(\rho k)}{\partial t} + \frac{\partial(\rho \overline{u}_i k)}{\partial x_i} = \frac{\partial}{\partial x_j}\left[(\mu + \sigma_k \mu_t)\frac{\partial k}{\partial x_j}\right] + \tau_{ij}\frac{\partial \overline{u}_i}{\partial x_j} - \beta^* \rho \omega k \quad \text{(Eq. 7)}$$

$$\frac{\partial(\rho \omega)}{\partial t} + \frac{\partial(\rho \overline{u}_i \omega)}{\partial x_i} = \frac{\partial}{\partial x_j}\left[(\mu + \sigma_\omega \mu_t)\frac{\partial \omega}{\partial x_j}\right] + \frac{\gamma}{\nu_t}\tau_{ij}\frac{\partial \overline{u}_i}{\partial x_j} - \beta \rho \omega^2 + 2\rho(1 - F_1)\sigma_{\omega 2}\frac{1}{\omega}\frac{\partial k}{\partial x_j}\frac{\partial \omega}{\partial x_j} \quad \text{(Eq. 8)}$$

$$\mu_t = \frac{\rho k}{\omega} \quad \text{(Eq. 9)}$$

Here, ω is the specific dissipation rate (s^{-1}) and ν_t is the kinematic turbulent viscosity ($\nu_t = \frac{\mu_t}{\rho}$ — measured in m^2 s^{-1}). Additionally, σ_k, σ_ω, and $\sigma_{\omega 2}$ are model constants; β and β^* are model constants related to dissipation; γ is a constant associated with controlling turbulence production; and F_1 is a blending function used in the SST model to transition between the $k-\omega$ and $k-\epsilon$ regions. All model constants and the blending function are dimensionless quantities.

The model was selected because it blends the strengths of $k-\omega$ in near wall regions, where it captures boundary-layer behaviour, and it accurately predicts adverse pressure gradients, with the robustness of $k-\epsilon$ in the free-stream region (12, 13). Furthermore, a study conducted by Douvi et al. (14) investigated the accuracy of different turbulence models, namely, Spalart-Allmaras, $k-\epsilon$, and $k-\omega$ SST by comparing values of coefficient of drag and lift to experimental values reported by Abbott and von Doenhoff (3) as well as Johansen (15) for the NACA 0012 airfoil; the authors of the study concluded that the $k-\omega$ SST model was most suitable as it reported data in good agreement with published experimental results. It is important to

note that no transition model (e.g., the $\gamma - Re_\theta$ model) was employed in this study; instead, fully turbulent flow was assumed from the leading edge for all simulations. As a result, the natural transition delay characteristic of laminar flow airfoils is not explicitly captured.

Airfoil Selection

In order to effectively compare the aerodynamic performance of traditional and laminar flow airfoils, this study presents a representative group of airfoils categorized as traditional and modern laminar flow. NACA 2412 and NACA 0012 represent the "traditional" group, as they belong to the NACA 4- and 5-series families — airfoils developed in the 1930s and 1940s during the early stages of systematic airfoil design, when theoretical understanding was limited and development relied heavily on wind-tunnel testing (3). These sections are widely regarded as conventional baselines in aerodynamic literature and have extensive experimental data available, making them suitable for validation purposes. Additionally, NACA 64A010 and NACA 747A315 were chosen to characterize the "laminar flow" group as the former belongs to the NACA 6-series family which was developed specifically to maintain laminar boundary layers and the latter is a member of the NACA 7-series family, which demonstrated greater extents of laminar flow along their upper and lower surfaces (3, 16).

Data Extraction

In the present 2-Dimensional, steady CFD simulation, the aerodynamic lift and drag were evaluated. Drag is the component of the net aerodynamic force parallel to the relative wind direction, and lift is the component perpendicular to free-stream velocity (17). The turbulence flow regime is characterized by the Reynolds number (*Re*) — a dimensionless parameter quantifying the ratio between inertial and viscous forces (18):

$$Re = \frac{\rho U_\infty c}{\mu} \qquad \text{(Eq. 10)}$$

Here, ρ is the free-stream density (kg m^{-3}), is the free-stream velocity (m s^{-1}), c is the chord length (m), and μ is the dynamic viscosity (kg m^{-1} s^{-1}). In addition to the Reynolds number, another key parameter governing airfoil dynamics is the angle of attack (measured in degrees), defined as the angle between the incoming free-stream velocity and the airfoil chord line. Together, *Re*, α, and the Mach number define the flow regime. To vary flight conditions, four different *Re*'s were used: 5×10^4, 5×10^5, 2×10^6, and 9×10^6 to represent low, moderate, and high turbulence flow conditions. Additionally, the angle of attack was varied from −16° to 20° at 4° intervals by changing the angle of the incoming free-stream, as this range captured the full range of pre-stall, stall, and post-stall behavior of the airfoils. The 4° interval provides sufficient resolution to observe trends in lift and drag curves without sacrificing unnecessary computational cost.

In this study, the net aerodynamic force was calculated using the following equation presented in tensor form,

$$F_i = \int_S \left(-p\, n_i + \tau_{ij} n_j\right) \mathrm{d}S \qquad \text{(Eq. 11)}$$

where F_i is the *i*-th component of the total aerodynamic force (N), τ_{ij} is the viscous stress tensor (Pa), n_j is the outward unit normal vector (dimensionless) to the surface S, and dS is a differential surface element (m^2). Then, the lift and drag was determined by decomposing the net force into components perpendicular and parallel to the free stream velocity using Eq. 12.

$$L = -F_x \sin\alpha + F_y \cos\alpha$$
$$D = F_x \cos\alpha + F_y \sin\alpha \qquad \text{(Eq. 12)}$$

Here, F_x (N) and F_y (N) are the total aerodynamic forces in the *x* and *y* directions (obtained from integrating pressure and shear stresses), L is the lift force (N), and D is the drag force (N). To allow comparison across flow conditions and geometries, results are expressed in terms of non-dimensional aerodynamic coefficients. Specifically, the coefficient of lift C_L and the coefficient of drag C_D:

$$C_L = \frac{L}{\frac{1}{2}\rho U_\infty^2 c} \; C_D = \frac{D}{\frac{1}{2}\rho U_\infty^2 c} \qquad \text{(Eq. 13)}$$

The dimensionless ratio C_L/C_D is further used as a measure of aerodynamic efficiency.

Steady Vs. Unsteady Flow

Steady flow occurs when all relevant flow variables (such as velocity and pressure) are invariant with time (17). Mathematically, the time derivatives of all flow quantities vanish, such that

$$\frac{\partial p}{\partial t} = 0, \;\; \frac{\partial u_i}{\partial t} = 0 \qquad \text{(Eq. 14)}$$

Accordingly, the incompressible steady-state Navier–Stokes equations in tensor form are expressed as

$$\frac{\partial u_i}{\partial x_i} = 0 \qquad \text{(Eq. 15)}$$

$$u_j \frac{\partial u_i}{\partial x_j} = -\frac{1}{\rho}\frac{\partial p}{\partial x_i} + \nu \frac{\partial^2 u_i}{\partial x_j \partial x_j} \qquad \text{(Eq. 16)}$$

Eq. 15 enforces mass conservation (continuity), while Eq. 16 represents the momentum balance with the unsteady term omitted.

The choice between steady or unsteady flow heavily depends on boundary layer attachment; in an attached flow regime, the boundary layer follows the airfoil camber with little or no separation resulting in drag and lift forces which change minimally in time. Therefore, steady state flows are justified as a good approximation of mean aerodynamic behavior because under the conditions being studied, air flow is mostly attached and quasi-steady. This approach offers computational efficiency while capturing dominant aerodynamic characteristics and neglecting minor effects, such as wakes and vorticies, at most of the and values.

Computational Fluid Domain and Auxiliary Conditions

To accurately capture fluid flow, airfoil geometries were imported from Airfoil Tools — all with a chord length of 1m — into Ansys Fluent, and a two-dimensional C-grid domain was constructed with a radius of 7.5m and a rectangular domain of width 15m. Appropriate boundary conditions were applied as velocity inlet, pressure outlet, and the airfoil is defined as a wall with a no slip condition, as shown in Figure 1, with the meshing parameters specified in Table 1.

Mesh Independence and Resolution

A mesh independence study was conducted for the NACA 2412 airfoil at $Re = 2 \times 10^6$ using three different mesh refinement levels (coarse, medium, and fine), as shown in Figure 2A, Figure 2B, and Figure 2C, respectively.

Plots of C_L vs. α and C_D vs. C_L for each grid type as well as experimental data were reported as shown in Figure 3A and Figure 3B, respectively. Each graph was close to the experimental data, proving that the numerical solution is not an artifact of grid size, and that mesh independence had been achieved.

Furthermore, the domain was divided into six faces with edge sizings defined with biases towards the airfoil, providing very refined near wall cells. The boundary layer was ensured to be very refined and the dimensionless wall distance y^+ was calculated. This parameter quantifies the non-dimensional distance from the wall to the first cell centroid and is defined as,

$$y^+ = \frac{u_\tau y}{\nu} \qquad \text{(Eq. 17)}$$

where u_τ is the friction velocity (m s^{-1}), y is the physical distance from the wall to the first grid point (m), and ν is the kinematic viscosity (m^2 s^{-1}). Maintaining a $y^+ \leq 1$ captures the viscous sublayer and allows the turbulence model to directly resolve near-wall effects without relying on wall functions. In this study, the near-wall mesh was

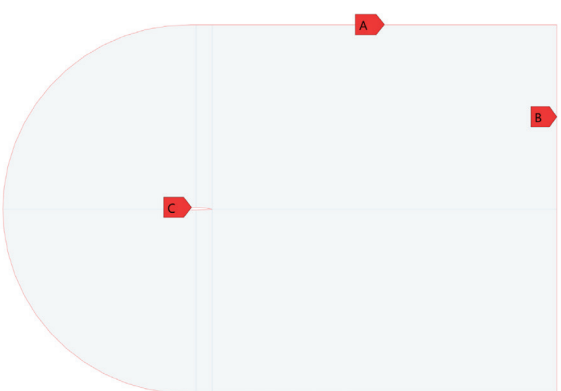

Figure 1. *Two-dimensional C-grid flow domain used in the simulations. Boundary conditions were specified as (A) velocity inlet, (B) pressure outlet, and (C) no-slip wall corresponding to the airfoil surface.*

Table 1. *Edge sizing parameters for different mesh densities across key regions of the computational domain.*

Region	Parameter Type	Coarse Mesh	Medium Mesh	Fine Mesh
Far-field arc	Number of divisions	50	100	200
Airfoil Surface	Number of divisions	50	150	300
Near-wake region	Number of divisions	50	150	300
Downstream edges	Number of divisions	100	250	500

refined such that $y^+ \leq 1$ was attained across all simulated cases. The y^+ distributions were also plotted for the NACA 2412 airfoil at $\alpha = 0°$ for the coarse, medium, and fine meshes, as shown in Figure 4. The medium mesh was selected for all simulations as the best compromise between achieving $y^+ \leq 1$ and minimizing computational time and resource consumption.

Validation

Validation of the numerical methodology was performed by comparing the computed aerodynamic coefficients with experimental data from established literature. Furthermore, Validation was carried out at one *Re* for each airfoil (where data was available) as a representative case to check that the CFD setup agrees with experimental data. After this check, the same CFD setup is applied to compute results at the other Reynolds numbers being studied. For the NACA 2412 airfoil, the simulation results were validated against the experimental measurements of Abbott, von Doenhoff, and Stivers (19) at a Reynolds number of 3.1×10^6, with the C_L vs. α comparison shown in Figure 5A. The NACA 0012 airfoil was validated using the data of Ladson (20) at $Re = 2 \times 10^6$, where the lift coefficient variation with angle of attack was compared as shown in Figure 5B. Similarly, the NACA 64A010 airfoil was validated against the results of Loftin (21) at $Re = 3 \times 10^6$, using C_L vs. α data as presented in Figure 5C. Finally, the NACA 747A315 airfoil validation employed experimental results from Abbott, von Doenhoff, and Stivers (19) at $Re = 3 \times 10^6$, also through C_L vs. α comparison as displayed in Figure 5D. Overall, close agreement between the numerical predictions and experimental data across these cases establishes confidence in the reliability of the CFD setup and turbulence model.

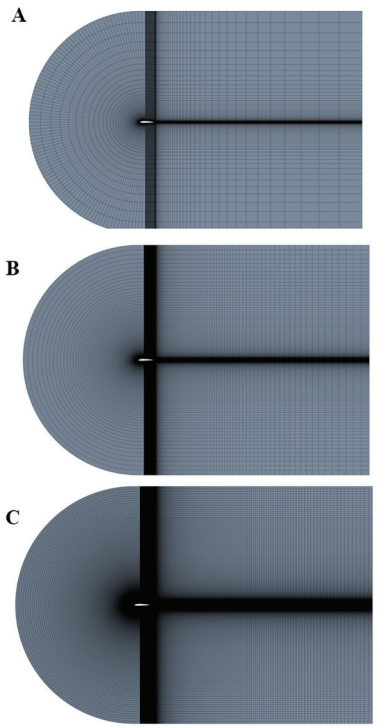

Figure 2. *Comparison of coarse, medium, and fine mesh configurations (with the NACA 2412 airfoil) used for the mesh independence study. (A) represents the coarse mesh, (B) represents the medium mesh, and (C) represents the fine mesh.*

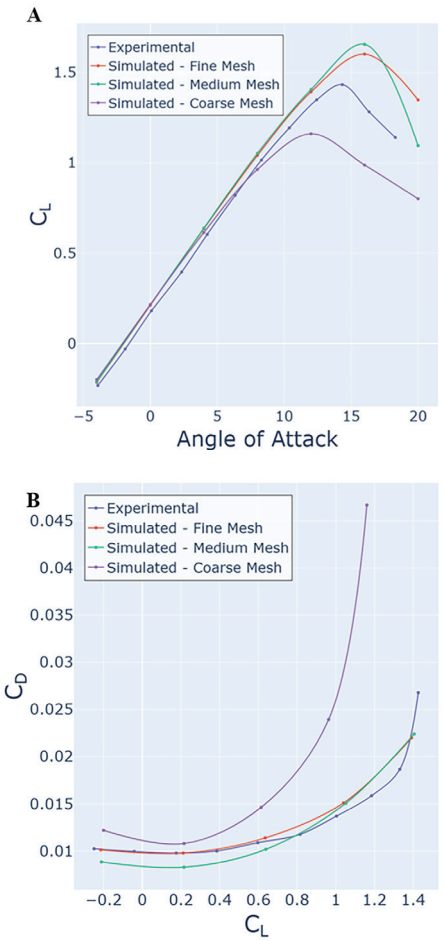

Figure 3. *Mesh independence validation for the NACA 2412 airfoil at different mesh resolutions (coarse, medium, and fine) at one Reynolds number (Re): (A) comparison of simulated and experimental lift coefficient (C_L) as a function of angle of attack (α) at $Re = 2 \times 10^6$, over angles of attack ranging from $\alpha = -4°$ to 20°; (B) comparison of simulated and experimental drag coefficient (C_D) as a function of lift coefficient (C_L) at $Re = 2 \times 10^6$.*

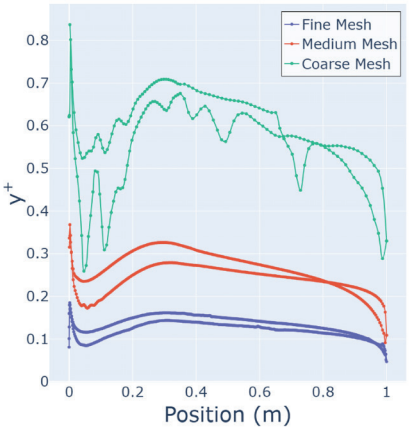

Figure 4. *Distribution of dimensionless wall distance (y^+) as a function of the chordwise position (m) along the airfoil surface for the coarse, medium, and fine meshes for the NACA 2412 airfoil.*

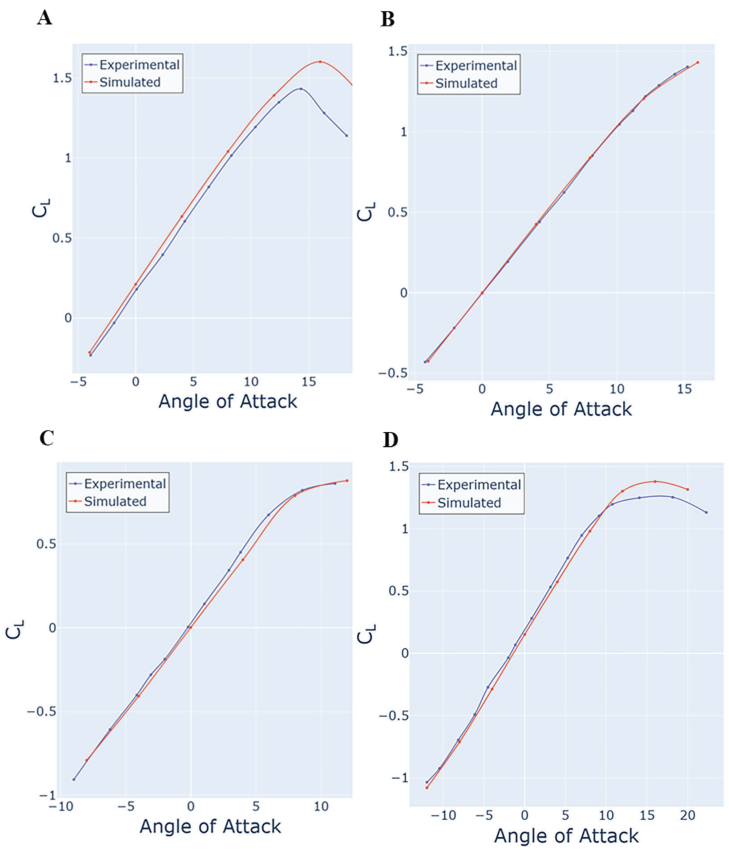

Figure 5. *Validation of the CFD methodology through comparison of simulated and experimental lift coefficient (C_L) as a function of angle of attack (α) for all airfoils (NACA 2412, NACA 0012, NACA 64A010, and NACA 747A315), evaluated at one Reynolds number (Re) for each airfoil where experimental data was available: (A) Simulated and experimental C_L vs. α curves for NACA 2412 at Re = 3.1 × 10⁶, over angles of attack ranging from α = −4° to 20°; (B) Simulated and experimental C_L vs. α curves for NACA 0012 at Re = 2.0 × 10⁶, over angles of attack ranging from α = −4° to 16°; (C) Simulated and experimental C_L vs. α curves for NACA 64A010 at Re = 3.0 × 10⁶, over angles of attack ranging from α = −8° to 12°; and (D) Simulated and experimental C_L vs. α curves for NACA 747A315 at Re = 3.0 × 10⁶, over angles of attack ranging from α = −12° to 20°. The close agreement between the simulated and experimental C_L vs. α curves across all cases demonstrates the accuracy of the numerical setup and turbulence modeling approach.*

RESULTS AND DISCUSSION

Figure 6 summarizes the simulated aerodynamic efficiency (C_L/C_D) trends across the different Reynolds numbers being studied. At $Re = 5 \times 10^4$, viscous effects dominate and all sections exhibit relatively high drag. In this regime, the NACA 2412 achieved the highest efficiency, reaching a maximum $C_L/C_D \approx 26$ at $\alpha = 8°$, followed by the NACA 0012 with a maximum $C_L/C_D \approx 22$ at $\alpha = 8°$. The laminar flow sections performed less efficiently at low *Re*, with the NACA 64A010 and NACA 747A315 reaching maximum C_L/C_D values of approximately 18 and 17, respectively, at $\alpha = 4°$. At $Re = 5 \times 10^5$, aerodynamic efficiency improved for all airfoils: the conventional sections reached peak $C_L/C_D \approx$ 45–55, while the laminar profiles reached approximately $C_L/C_D \approx$ 30–40 (Figure 6B). Overall, at low-to-moderate Reynolds numbers (5×10^4 to 2×10^6), the laminar flow airfoils consistently produced lower peak C_L/C_D than the conventional sections (Figure 6A–6C). This result can be explained by low-*Re* airfoil behaviour, where reduced near-wall momentum thickens the boundary layer and increases profile losses, degrading efficiency for sections designed to realize benefits primarily at higher Reynolds numbers (3, 17). This data at low *Re* values is consistent with established aerodynamic theory, as the laminar flow airfoils used in the present study are optimized for 3×10^6 to 9×10^6 *Re* (21, 16).

At $Re = 9 \times 10^6$, the NACA 2412 produced the highest lift-to-drag ratio ($C_L/C_D \approx 90$ at $\alpha = 8°$), followed by the NACA 747A315 ($C_L/C_D \approx 79$ at $\alpha = 8°$), then the NACA 0012 ($C_L/C_D \approx 77$ at $\alpha = 8°$), and finally the NACA 64A010 ($C_L/C_D \approx 62$ at $\alpha = 8°$), as shown in Figure 6D. Laminar flow airfoils can exhibit a low-drag "bucket" around their design lift coefficient, but this advantage is typically confined to a narrow operating range and is sensitive to surface conditions (17). In contrast, the traditional airfoils maintained stronger overall efficiency

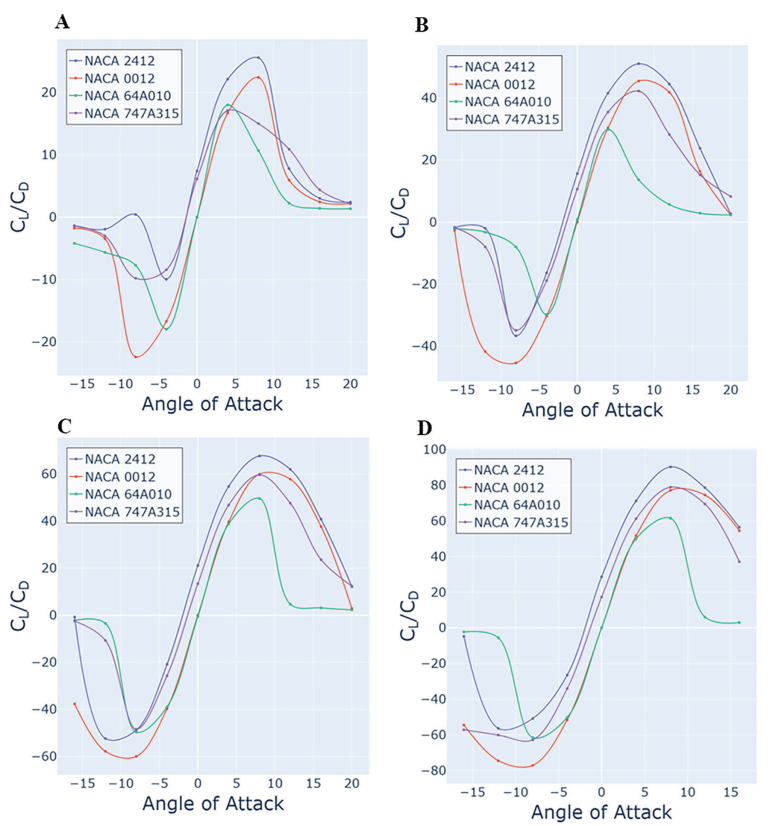

Figure 6. *Variation of simulated lift-to-drag ratio (C_L/C_D) with angle of attack (α) for all airfoils (NACA 2412, NACA 0012, NACA 64A010, NACA 747A315) across different Reynolds numbers (Re). (A) presents simulated C_L/C_D vs. α at $Re = 5 \times 10^4$, over angles of attack ranging from $\alpha = -16°$ to 20°; (B) presents simulated C_L/C_D vs. α at $Re = 5 \times 10^5$, over angles of attack ranging from $\alpha = -16°$ to 20°; (C) presents simulated C_L/C_D vs. α at $Re = 2 \times 10^6$, over angles of attack ranging from $\alpha = -16°$ to 20°; and (D) presents simulated C_L/C_D vs. α at $Re = 9 \times 10^6$, over angles of attack ranging from $\alpha = -16°$ to 16°.*

across the measured angles of attack, consistent with their more robust performance over a broader lift range. Additionally, laminar flow sections are expected to have lower maximum lift coefficients than conventional sections (22); the experimental data produced by Abbott, von Doenhoff, and Stivers (19) for the NACA 2412 and NACA 747A315 (Figure 7) supports this qualitative conclusion. Consequently, even at high Reynolds numbers, the laminar flow sections in this study did not surpass the best performing conventional section in peak efficiency, despite their design intent of reducing profile drag (3).

Post-stall, the laminar flow sections exhibited a more gradual decline in lift (as evident in Figure 8) with increasing angle of attack compared to traditional airfoils. This slower rate of lift decay observed in laminar flow airfoils can be attributed to their more gradual flow separation characteristics compared to traditional airfoils. This behavior can be beneficial for applications requiring stable post-stall handling and smooth stall-onset, such as UAVs and trainer aircraft (3). However, it also typically results in reduced high α performance, which may be a significant drawback in maneuver-focused designs (23). Consequently, while the post-stall stability of laminar flow sections is improved, their peak aerodynamic performance is inherently limited.

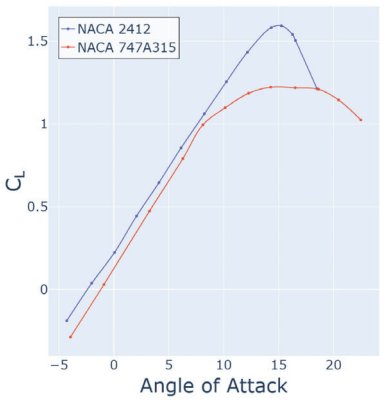

Figure 7. *Experimental lift coefficient (C_l) vs. angle of attack (α) at a Reynolds number (Re) of 9 × 10⁶ for the NACA 2412 and NACA 747A315 airfoils, over angles of attack ranging from α = −4° to 16°. The data shown is produced from the experimental measurements reported in Ref. 19.*

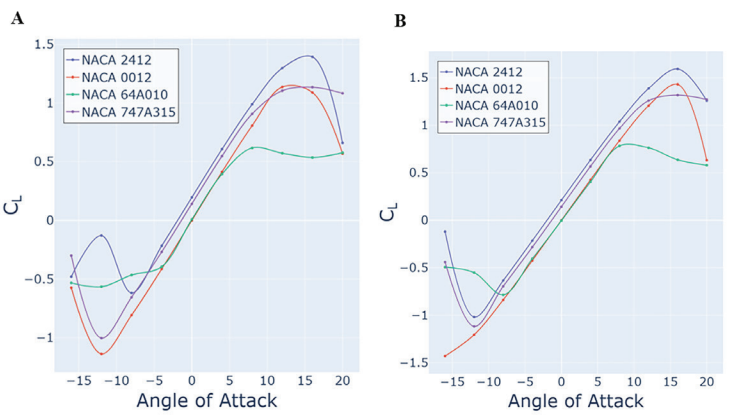

Figure 8. *Simulated coefficient of lift (C_l) vs. angle of attack (α) across all airfoils (NACA 2412, NACA 0012, NACA 64A010, NACA 747A315) at Reynolds numbers (Re) of 5 × 10⁵ and 2 × 10⁶. (A) presents the simulated C_L vs. α plot at Re = 5 × 10⁵, over angles of attack ranging from α = −16° to 20° and (B) presents the simulated C_L vs. α plot at Re = 2 × 10⁶, over angles of attack ranging from α = −16° to 20°.*

CONCLUSION

The primary objective of this study was to investigate the aerodynamic performance trade-offs between laminar flow and traditional airfoils across varying Reynolds numbers using CFD analysis. The results demonstrated that the traditional NACA 2412 and NACA 0012 airfoils consistently achieved higher lift-to-drag ratios across all simulated Reynolds numbers. The NACA 2412 airfoil exhibited the highest overall C_L/C_D values, maintaining aerodynamic efficiency even at low Reynolds numbers (5×10^4), while the laminar flow airfoils (NACA 64A010 and NACA 747A315) showed comparatively lower performance. Only at $Re = 9 \times 10^6$ did the NACA 747A315 marginally surpass the NACA 0012 in C_L/C_D, but remained below the NACA 2412. The modern laminar flow sections did, however, exhibit a slower rate of decay of the lift coefficient post-stall. These findings suggest that engineers selecting or designing airfoils for applications demanding consistent performance across a wide array of *Re*'s may favor designs resembling that of traditional sections due to their persistently higher maximum efficiency. Nevertheless, the slower post-stall decrease of laminar flow airfoils may be advantageous in specific applications like UAVs and trainer aircraft, where smoother stall characteristics are desirable. Future research should incorporate a broader range of airfoil geometries to better represent both laminar flow and traditional categories and investigate the performance at *Re* at higher values than used in this study. Experimental validation could also enhance the accuracy of results, as the current study relied solely on numerical turbulence models. Exploring three-dimensional effects such as induced drag and wing aspect ratio influence would provide a more comprehensive understanding of practical aircraft performance. This study is constrained by the use of a two-dimensional CFD approach, which neglects spanwise flow and tip effects inherent in real wings. Moreover, the study assumes fully turbulent flow and does not explicitly model laminar-turbulent transition, limiting the accuracy of conclusions made on the performance of laminar flow airfoils. Furthermore, only four airfoils were analyzed, which limits the generalization of conclusions across broader laminar flow and traditional airfoil families. Finally, turbulence modeling and numerical discretizations introduce inherent uncertainty, particularly at high angles of attack where convergence was less robust.

CONFLICT OF INTEREST

The author declares no conflicts of interest related to this work.

REFERENCES

1. Punke JO. A Review and Study on Airfoils and Aerodynamics. *National High School Journal of Science (NHSJS)*. 2024: 1-10.
2. Paredes P, Mysore P, Jacobson K, Diskin B, Hildebrand NJ, Choudhari MM. Aerodynamic Design Optimization for Natural Laminar Flow Airfoils. In: AIAA AVIATION FORUM AND ASCEND 2024; 2024: 3529. https://doi.org/10.2514/6.2024-3529
3. Abbott IH, Von Doenhoff AE. Theory of Wing Sections: Including a Summary of Airfoil Data. Dover Publications; 1959. ISBN: 978-0486605869.
4. Dantsker OD, Selig MS. High Angle of Attack Flight of a Subscale Aerobatic Aircraft. In: 33rd AIAA Applied Aerodynamics Conference; 2015; p.2568. https://doi.org/10.2514/6.2015-2568
5. Selig MS, Maughmer MD, Somers DM. Natural-Laminar-Flow Airfoil for General-Aviation Applications. *Journal of Aircraft*. 1995; 32 (4): 710-5. DOI: https://doi.org/10.2514/3.46781.
6. Winslow J, Otsuka H, Govindarajan B, Chopra I. Basic Understanding of Airfoil Characteristics at Low Reynolds Numbers (104-105). *Journal of Aircraft*. 2018; 55 (3): 1050-61. DOI: https://doi.org/10.2514/1.C034415.
7. Versteeg HK. An Introduction to Computational Fluid Dynamics: The Finite Volume Method. Pearson Education; 2007. ISBN: 978-0131274983.
8. Xiao H, Cinnella P. Quantification of Model Uncertainty in RANS Simulations: A Review. *Progress in Aerospace Sciences*. 2019; 108: 1-31. DOI: https://doi.org/10.48550/arXiv.1806.10434.
9. ANSYS Fluent. Ansys Fluent Theory Guide; 2024. Ansys Inc. Available from: https://ansyshelp.ansys.com/ (accessed 2025-9-25).
10. Tennekes H, Lumley JL. A First Course in Turbulence. MIT press; 1972. ISBN: 978-0262200196. https://doi.org/10.7551/mitpress/3014.001.0001
11. Menter FR. Improved Two-Equation k− ω Turbulence Models for Aerodynamic Flows. Moffett Field, California, USA. 1992. https://doi.org/10.2514/6.1993-2906
12. SimScale. k− ω SST Turbulence Model - Global Settings, SimScale Documentation; 2025. Available from: https://www.simscale.com/docs/simulation-setup/global-settings/k-omega-sst/ (accessed 2025-10-19).

13. Menter FR. Two-Equation Eddy-Viscosity Turbulence Models for Engineering Applications. *AIAA journal*. 1994; 32 (8): 1598-605. DOI: https://doi.org/10.2514/3.12149.
14. Douvi EC, Tsavalos AI, Margaris DP. Evaluation of the Turbulence Models for the Simulation of the Flow over a National Advisory Committee for Aeronautics (NACA) 0012 Airfoil. *Journal of Mechanical Engineering Research*. 2012; 4 (3): 100-11. https://doi.org/10.5897/JMER11.074
15. Johansen J. Prediction of Laminar/Turbulent Transition in Airfoil Flows; 1997. ISBN: 87-550-2308-8.
16. Von Doenhoff AE, Stivers LS. Aerodynamic Characteristics of the NACA 747A315 and 747A415 Airfoils from Tests in the NACA Two-Dimensional Low-Turbulence Pressure Tunnel. National Advisory Committee for Aeronautics; 1944. ISBN: 978-1013881909.
17. Leishman JG. Introduction to Aerospace Flight Vehicles. Embry-Riddle Aeronautical University; 2023. ISBN: 979-8-9852614-0-0.
18. LaNasa PJ, Upp EL. Fluid Flow Measurement: A Practical Guide to Accurate Flow Measurement. Butterworth-Heinemann; 2014. ISBN: 978-0124095243. https://doi.org/10.1016/B978-0-12-409524-3.00003-4
19. Abbott IH, Von Doenhoff AE, Stivers Jr L. Summary of Airfoil Data; 1945.
20. Ladson CL. Effects of Independent Variation of Mach and Reynolds Numbers on the Low-Speed Aerodynamic Characteristics of the NACA 0012 Airfoil Section. vol. 4074. National Aeronautics and Space Administration; 1988. ISBN: 978-1730943355.
21. Loftin Jr LK. Theoretical and Experimental Data for a Number of NACA 6A-Series Airfoil Sections; 1946.
22. Cantwell BJ. The NACA Airfoil Series; 2013. Course material, AA200 Applied Aerodynamics, Dept. of Aeronautics & Astronautics, Stanford University. Available from: https://web.stanford.edu/~cantwell/AA200_Course_Material/The%20NACA%20airfoil%20series.pdf (accessed 2025-10-19).
23. McMasters J, Henderson M. Low-Speed Single-Element Airfoil Synthesis. *Technical Soaring*. 1980; 6 (2): 1-21.